Metascience in Aerospace

Metascience in Aerospace, 2(4): 89–109.
DOI: 10.3934/mina.2025005
Received date: 18 August 2025
Revised date: 20 October 2025
Accepted date: 20 November 2025
Published date: 28 November 2025

https://www.aimspress.com/journal/mina

Research article

The Effect of Gravity on Heat Transfer and Species Composition for a Concurrent Flame over a Liquid Surface Subjected to a Low-Speed Flow

Hui Ying Wang* and Anh Quan Nguyen

Institut Pprime (CNRS-UPR 3346, ENSMA, Poitiers University), BP 40109, Téléport 2, 1 av Clément ADER, 86961 Futuroscope Chasseneuil Cedex, France

* **Correspondence:** Email: wang@ensma.fr; Tel: 335-4949-8295.

Abstract: In this theoretical study, we dealt with the impact of gravity on flame shape, heat flux, and species composition in laminar diffusion flame subjected to a low-speed flow of 0.2 m/s with an oxygen concentration of 25%. The visible flame length (600°C contour) over a flat liquid surface in microgravity environments was substantially longer by a factor of 2.5 times than the flame height on Earth. Our results showed that with the presence of a backward-facing step in front of a fire, the flame length in microgravity decreased significantly by a factor of 5 times, which was different from the height of a buoyancy-induced fire. In microgravity, the soot-related radiation was a predominant mode of heat transfer except at the leading edge, resulting in a large and consistent radiative loss fraction above 0.5. The heat feedback from a microgravity flame to the fuel surface was two times smaller than that on Earth and decreased further with the presence of a backward-facing step in front of a fire. These findings implied that at a low-speed flow, there could be a higher toxic emission in microgravity than these on Earth. The longer flame tail and the higher toxic productions in microgravity would have significant implications for spacecraft fire safety.

Keywords: microgravity flame; buoyancy-induced fire; heat flux; pyrolysis rate; species composition

1. Introduction

Since the time spent on board a spacecraft is increased due to the operation of proposed space missions, a fire safety strategy is used to prevent ignition of thermally destructing materials that are

directly above or adjacent to a heat source [1]. In the context of a measure of the fire hazard, fire growth rate is controlled by ignitability of condensed materials, which is associated with heat transfer and species composition. In a spacecraft, a gas flow velocity of about 0.2 m/s is induced by a HVAC system [2], and such flow is significantly weaker than the fire-entrained buoyant flow on Earth. Flame behaviors are very different in a spacecraft from those on Earth at a low-speed flow. From an opposed flame spread over a PMMA rod, the microgravity flame is with a smaller tail and a larger width; however, buoyant convection driven by the flame on Earth enables the flame to contract and enlarge [3]. For a condensed fuel exposed to an external radiant flux, the ignition delay under reduced gravity and in low-speed flows is shorter than that on Earth [4]. The downward flame spread and heat flux over solid fuel become insensitive to an applied opposed flow on Earth due to a stable pyrolysis rate of the condensed fuel, as observed in [5]. The buoyancy-induced flow is conducted to blow-off of an upward flame spread over thin solid materials [6]. Moreover, the curvature effect on microgravity flame spread rate over solid fuel is studied via enhanced convective heat transfer [7]. There is self-similar solution [8] to a flame spread over condensed fuel solely in the case where the convective heat feedback is predominant at very-high-flow speed. With the suppression of buoyancy, radiative exchanges between flame, solid fuel, and environment become predominant for the flame growth in a very mild flow field [9]. The three-dimensional computations are uncoupled with gas radiation by excluding soot emission in flame [10]. Impact of ambient pressure at microgravity on an opposed flame spread over an electrical wire is assessed [11]. By applying an electric field in a microgravity flame, any feedback between ion-driven convection and reacting behavior is captured [12]. The opposed flame spread over thin cellulosic fuels is studied on Earth and at microgravity thanks to a drop tower facility [13].

Many liquid lubricants could originate from leaking machinery on board a spacecraft. Typically, the ignition temperature of liquid fuel is smaller than that of solid fuel, thus a flame growth over a liquid surface is quicker compared to that over a solid surface [14]. Predictions and experiments show that a forced airflow is needed to sustain flame spread over liquids in microgravity, while the flame sustains itself in a pulsating mode on Earth [15]. The consequences of forced airflow on flame spread rate over butanol in microgravity is moderate, and on the flame pulsation frequency in normal gravity it is large due to buoyant convection [16]. Moreover, there was not a measurement methodology developed [15,16] to determine the liquid vaporization rate, heat flux over a liquid surface, and chemical species from a liquid fire in environments similar to those expected in spacecraft. The objective of this study is to understand further the consequences of gravity on flame structure, heat transfer, and species composition over liquid fuels, which are, to a large extent, unexplored. The soot-related radiation controlling the flame growth on Earth and in microgravity environments over a surface of heptane is taken into account. Although heptane may be never used in spacecraft, it is extensively used in an attempt to study flame destabilization and extinction [17,18,19]. A simple soot-yield conversion model [18] or no soot emission [19] cannot be applied to a heavily sooting, microgravity boundary layer flame. The innovation of this study lies in the implementation of a Laminar Smoke Point (LSP) model [20] in FDS6.8 [21], which has been evaluated thanks to quantitative comparisons of soot emissions in ethylene and heptane fires [22,23]. To identify the impact of the geometrical configuration on transport of oxygen and heat exchange in microgravity and in normal gravity, both a flat flame and a flame behind a backward-facing step are considered. Quantitative results on flame temperature, evaporation rate, combustion efficiency, radiative loss fraction, heat flux, and species composition are reported thanks to these numerical simulations.

2. Numerical modeling

Fire Dynamics Simulator (FDS6.8) [21] is used, and a Direct Numerical Simulation (DNS) is adopted to the simulations conducted throughout this study. A non-homogeneous combustion over thermally destructing material includes the interaction between the condensed phase and the gas phase [24]. In the gas-phase, the model consists of the three-dimensional Navier-Stokes equations for the conservation of mass, momentum, and energy in addition to species equations for fuel, O_2, H_2, CO, CO_2, H_2O, and soot. The physics-based equations that govern the phenomena of interest here are discretized and iteratively solved as described in detail in the FDS6.8 user guide [21].

Based on a multi-step, quasi-global mechanism, a three-step chemistry scheme is assumed for oxidation of heptane [25] in flames,

$$C_7H_{16} + 10O_2 \rightarrow 6\ CO_2 + 7\ H_2O + CO + H_2 \tag{1}$$

$$2\ CO + O_2 \leftrightarrow 2\ CO_2 \tag{2}$$

$$2\ H_2 + O_2 \leftrightarrow 2\ H_2O \tag{3}$$

To avoid the numerical modeling on ignition processes via finite-rate kinetic reactions, a mixed reaction is employed, including a fast chemistry for the heptane oxidation (Eq.1) and a finite-rate Arrhenius reverse reaction between CO/H_2 and O_2 (Eqs.2, 3) [21]. The net change of species in a time step along with the enthalpy of formation of each species enables the calculation of heat release rate in the energy equation.

For a heavily sooting flame, such as fire, both surface and gas radiations are taken into account in the model. The gas-phase Radiative Transfer Equation (RTE) is considered with the coupled computation of soot emission even though it is very time-consuming. The RTE is solved through a ray-based method [21] in angular discretization and a finite volume method in spatial discretization,

$$\vec{\nabla}.\vec{\Omega}I + \kappa I = \kappa\frac{\sigma T^4}{\pi} \tag{4}$$

The most important combustion products, such as H_2O, CO, CO_2, and soot, control the gas-phase thermal radiation via the absorption coefficient, κ, in Eq. 4.

$$\kappa = \kappa_s + \kappa_g \tag{5}$$

A spectral dependence of gas absorption coefficient, κ_g, is taken into account for the contribution from gas-phase radiation of H_2O, CO, and CO_2 [21]. Since the radiation spectrum of soot is continuous, its absorption coefficient is calculated from the gas temperature, T, and soot volume fraction, f_v [21].

$$\kappa_s = 1225 f_v T \tag{6}$$

The empirical calibration parameters in inception, coagulation, and surface growth processes for ethylene flame in the advanced soot modeling [26] cannot be directly applied to any condensed fuel. The more robust modeling framework as LSP is widely employed to calculate soot emission, C_s, in buoyancy-induced fire [22] and in a microgravity flame [23]. In this work, the LSP model is coupled with a three-step chemistry scheme to calculate the soot precursory rate from the gas temperature and mixture fraction. The pre-exponential factor in an Arrhenius reaction of soot precursory rate is reversely proportional to smoke height. The oxidation rate of soot, C_s, to CO_2 is determined from an

Arrhenius expression as a function of the gas temperature and the soot/oxygen concentrations via the following chemistry scheme [27]:

$$C_s + O_2 \rightarrow CO_2 \quad (7)$$

It is worth noting that such a quasi-global chemistry mechanism (Eqs. 1–3) cannot provide OH* and O* radicals in soot oxidation via the elementary reactions [27].

The Stefan equation is used to calculate the evaporation rate of heptane via the thermo-physical and combustion properties [25]. The liquid fuel with a thickness of 1 cm is considered thermally-thick, and a one-dimensional heat conduction equation is applied for the temperature stratification in the liquid phase. Heat balance through convective and radiative heat exchanges is established on the liquid front surface to calculate its temperature. Over the liquid surface, the radiation heat flux is calculated from the radiation intensity by solving RTE (Eq. 4), and the convective heat flux is determined from a Fourier law [21]. Mass fraction of fuel vapor at the interface is found from a Clausius-Clapeyron relation in an equilibrium state via liquid surface temperature [21].

3. Model evaluation from a microgravity ethylene flame

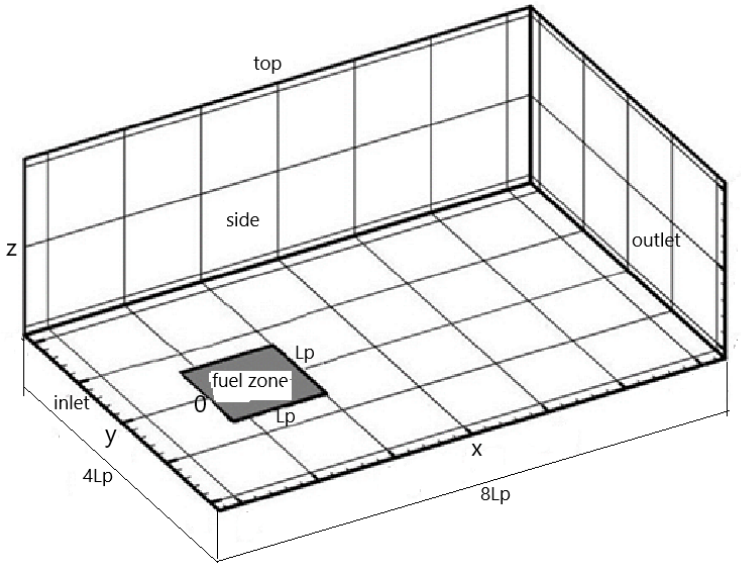

Figure 1. Schematic diagram of the experimental set-up and a computation coordinate system.

Schematic diagram of the fire configuration and the coordinate system in the computation are displayed in Figure 1. A laser induced incandescence technique (LII) [28] was developed to measure the soot volume fraction of an ethylene laminar diffusion flame at microgravity. The experiment concept and hardware design [28] during airplane flying parabolic trajectories provide model guidance for fuel size and oxidizer flow velocity. A square porous burner with a size of L_p=5 cm provides a gas fuel (ethylene) supply rate of 5 g/m^{2}s at the bottom (z=0), downstream an entrance of 5 cm. The computation domain is limited to $8L_p$ in the windward direction, and $4L_p$ in both the lateral and normal directions, enabling us to exclude the negative effect of boundary entrainment on a flow field. A highly compressed grid system, which has to be used for an excessive computation domain, induces a significant calculation error [21]. At the two sides and the top, free slip conditions for the velocity are

imposed. At the outlet of the domain, zero gradient conditions are applied. An oxygen mass fraction of Y_o=0.35 and a flow speed of U_o=0.2 m/s are prescribed at the inlet of $x/L_p = -1$. The initial temperature of 300 K is imposed for the gas fuel and the crossflow.

As shown in Figure 2(a), the experimental image [28] from a Canon digital camera is characterized by a boundary layer diffusion flame over a fuel surface at microgravity. The computed visible flame shape can be defined as the isotherm of 600°C with most of the soot-related radiation. Sooty area is represented by the yellow color due to soot glowing as opposed to blue, which is exposed directly to the leading edge with a weak soot emission. The interaction between soot and radiative heat loss becomes the primary factor translating a blue region with a high temperature to a yellow sooty region with a low temperature. A mesh sensitivity analysis on the visible flame shape by reducing the grid size from 2 to 1 mm is illustrated in Figure 2(b, c). Regardless of the mesh size, the predicted visible flame shape in length and thickness is similar to the experimental trend. The numerical uncertainty within 5% is observed only in the zone with a flame temperature of 1700°C at the leading-edge region with a reduction in the mesh size from 2 to 1 mm. A grid system contains 200 ×100 ×75 cells with a mesh size of 2 mm, and a physical time of 10 s needs about 150 CPU hours by using 10 processors of a Linux cluster. It is worth noting that with a reduction in the grid size from 2 to 1 mm, the computational time increases by a factor of two for each spatial coordinate, plus time for satisfying the CFL stability condition.

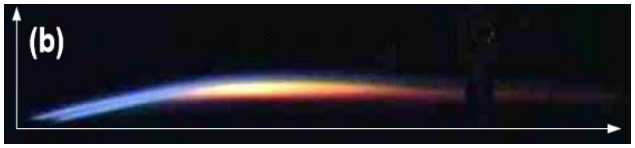

2a). Experimental image.

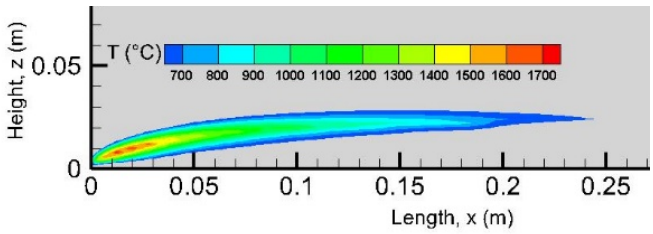

2b). Mesh size of 2 mm.

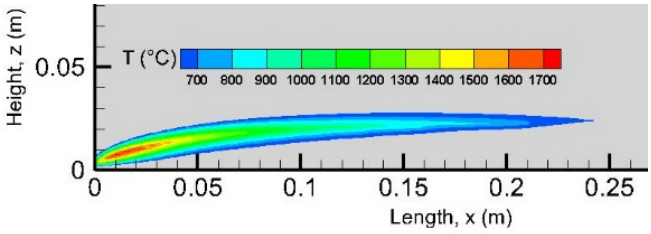

2c). Mesh size of 1 mm.

Figure 2. Qualitative comparison between the experimental image and the predicted iso-contour of a temperature above 600°C at U_0=0.2 m/s and Y_o=0.35.

The predicted soot volume fraction is compared with the measurements in Figure 3 and Figure 4 for the grid spacing of 2 and 1 mm across the height, z, at x/L_p=0.4, 0.8, 1.2, 1.6, 2, and 2.4. The predicted peak in soot volume fraction is deemed satisfactory compared to the experimental data. Indeed, an attempt to reduce the mesh size from 2 to 1 mm does not enable us to match the experimental data with every 0.2 mm at x/L_p=1.2 and 1.6. Regardless of an extremely small grid size of 1 mm, which enables us to fully resolve the flame sheet, the computation over-predicts the soot stratification thickness in the boundary layer by a factor of two times in the post combustion region. A systematic deviation between the prediction and the experiment is attributed not only to the errors induced by the cell size, but also to all the assumptions made in modeling and uncertainties in measurement at microgravity [28]. The OH* and O* radicals, which cannot be provided via a quasi-global chemistry mechanism (Eqs.1–3), play a dominant role for soot burnout in the post flame region, enabling us to reduce the soot stratification thickness. The discrepancy between the calculated and measured soot thickness might originate from neglecting the endothermicity in soot precursory reactions [28].

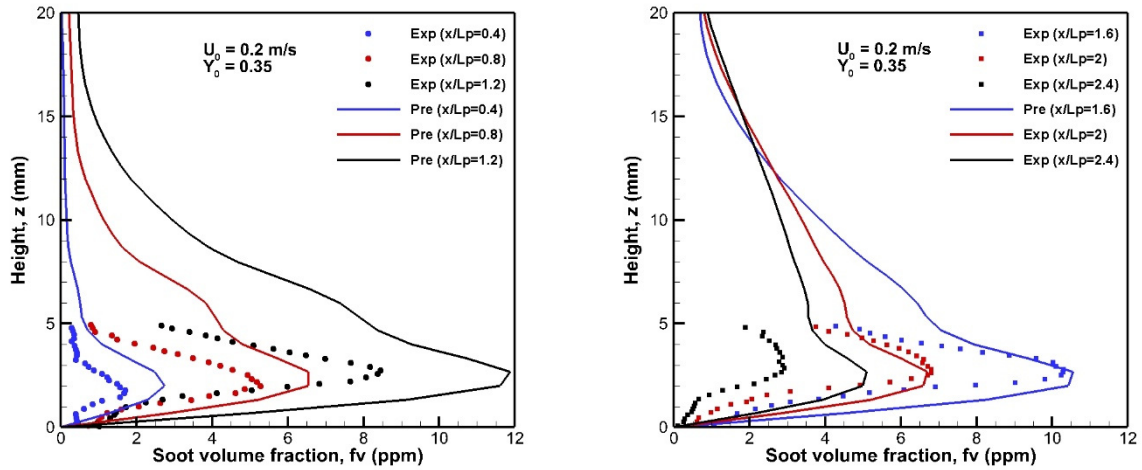

Figure 3. Comparison between the calculated and measured soot volume fraction along the height z at various positions with a grid spacing of 2 mm.

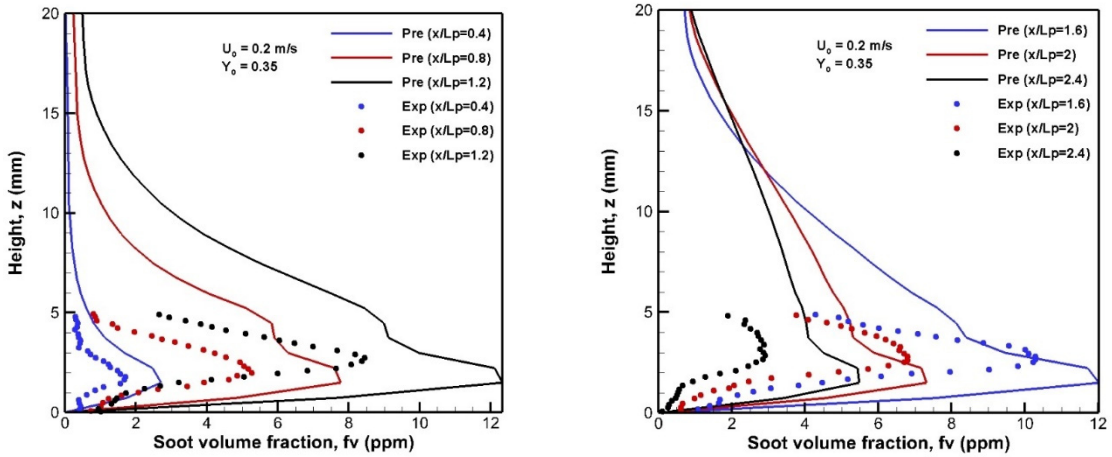

Figure 4. Comparison between the predicted and measured soot volume fraction at various axial locations with a mesh size of 1 mm.

4. Results and observations

The above study on ethylene flame (section 3) indicates that a grid size of 2 mm enables us to obtain a relatively good estimation of both the soot emission and the flame shape. Moreover, a mesh size of 2 mm is extensively used for a practical three-dimensional reacting flow simulation at low Reynolds number flow [23]. A fire growth asymptotically reaches a steady state during a physical time of about 20-45 s via heat feedback from a flame to liquid surface as a function of liquid temperature. A grid spacing of 2 mm is chosen, and roughly 300-500 CPU hours are required for each simulation of liquid pool fires. With each halving of the mesh size to 1 mm, a prohibitive CPU time with an increasing factor of 16 is required. In fact, the accurate prediction depends also on other factors such as soot, radiation, and combustion models with respect to the fire scenario related to fuel type, fire size, and ventilation conditions. All the results on flame shape, species, and heat flux are time-averaged over the last 1 s at a steady state for establishing a mean value.

The concurrent flame structure over a liquid surface subjected to a crossflow depends on a ratio between buoyant and inertia forces, defined as

$$\xi = \frac{\mathrm{Gr_x}}{\mathrm{Re_x^{5/2}}} \tag{8}$$

where $\mathrm{Re_x}$ and $\mathrm{Gr_x}$ denote the Reynolds number and the Grashof number, respectively [29]. A clear illustration is that of Figure 5 and Figure 6, which show flame structure in normal gravity and in microgravity. The axis, x, is normalized by the fuel size, L_p, to show the pyrolysis zone ($x/L_p=1$). According to an experimental photo, the yellow color in a flame is a consequence of soot radiation [30]. The blue color implies a lower soot emission in the flame or potential soot moving away from the reactive region [28]. On Earth, a small magnitude (0.2 m/s) of a forced flow results in a ratio (Eq. 8) much greater than unity, and a predominant natural convection generates a vertical thermal plume (Figure 5). The flame behavior subjected to a low-speed crossflow is slightly affected by a backward-facing step due to the dominant upward buoyancy-induced flow. Nevertheless, it may be inferred that a backward-facing step significantly reduces the flame temperature near the corner region (Figure 5b). In normal gravity, the predicted visible flame height, defined as the furthest axial position of the isotherm 600°C [22], is roughly 0.12 m. Near the bottom of the fire, the flame color is blue with negligible soot-related luminous radiation at the leading edge with a high temperature of 1200°C due to a large heat release from an exothermic reaction. In the middle section of the fire, the temperature is relatively low because little oxygen has penetrated a fuel-rich core to ensure an exothermic reaction. This is followed by a temperature decreasing region due to more entrained cold air, which induces an exponential decrease in the rate of chemical reactions. In microgravity, the ratio (Eq. 8) becomes much lower than unity, and a concurrent boundary layer diffusion flame (Figure 6) becomes the superior mode with a significant rise of the stand-off distance. A blue flame near the leading edge with a temperature of 1400°C and negligible soot emission changes to a yellow flame of the 600°C contour where soot particles are radiating heat [28]. A flat liquid surface in microgravity contributes to a long flame tail (600°C contour) with an increase by a factor of 2.5 times in flame length compared to the height of a buoyancy-induced pool-fire. It is seen that under reduced gravity environments, the flame structure changes particularly behind a backward-facing step where the oxygen-transport of low-speed flow limits the flame propagation [31] with a reduction in flame length by a factor of 5 times compared to that over a flat surface.

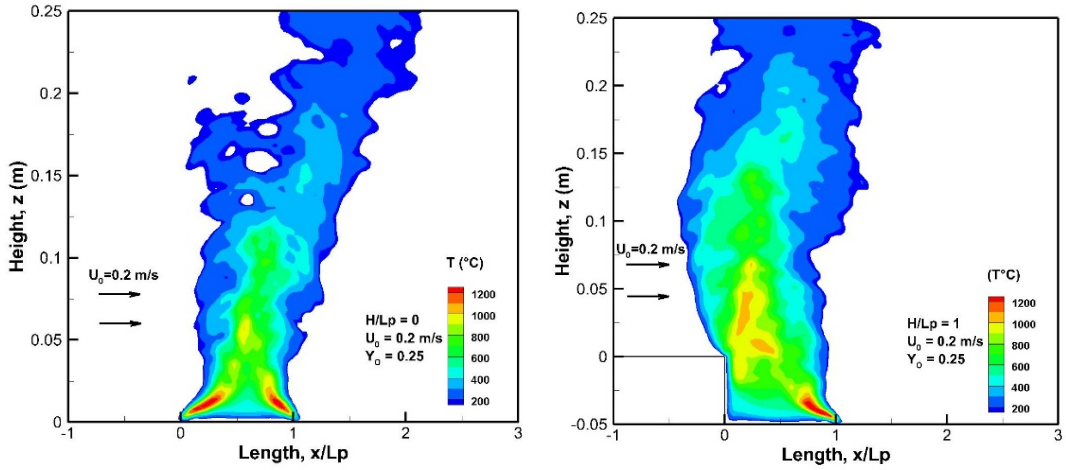

5a). Over a flat surface. 5b). Behind a backward-facing step.

Figure 5. Fields of gas temperature in normal gravity on the symmetrical plane (x, z).

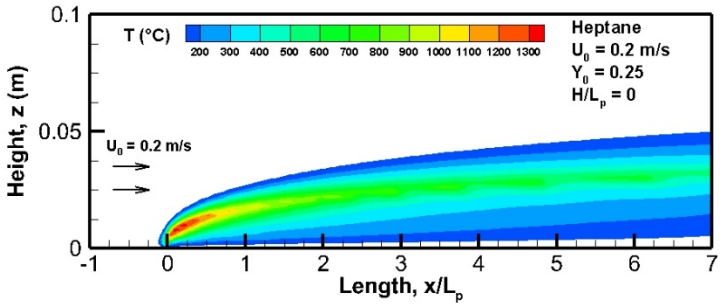

6a). Over a flat surface.

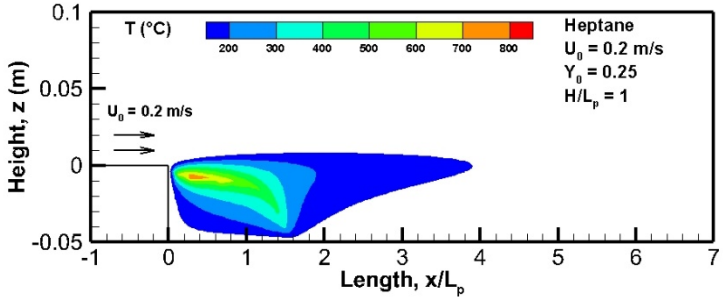

6b). Behind a backward-facing step.

Figure 6. Fields of gas temperature in microgravity on the symmetrical plane (x, z).

The convective and radiative heat feedback from the flame to the liquid surface are presented in Figure 7(a, b). For the buoyancy-induced fire, the convection heat flux is dominant with a peak of about 17 kW/m^2 near the leading edge and decreases sharply far from that region as a result of a

reduction in temperature gradient. In the middle section of the pyrolysis zone, a predominant natural convection yields substantial soot and luminous radiation [22]. A curvature effect of microgravity flames at the leading edge with a high flame temperature (Figure 6a) promotes a peak of roughly 20 kW/m^2 in convective heat flux. In both normal gravity and microgravity, downstream the leading edge or behind a backward-facing step, a significant flame lifting from the flat surface leads to a significant decrease in convective heat flux due to a reduction in the temperature gradient. In fact, the flame structure (Figure 6) dominates the distribution of the radiative and convective heat fluxes over the fuel surface. For a flat microgravity flame, the zone with a high radiative heat flux of about 4 kW/m^2 covers the pyrolysis area (Figure 7b). Behind a backward-facing step, the convective and radiative heat fluxes decrease drastically to about 1 kW/m^2 due to a shorter flame (Figure 6b). Under a reduced gravity, the radiative heat flux over a flat heptane surface augments by a factor of 8 times compared to that for the flame behind a backward-facing step (Figure 7b). The radiative flux is a temperature-sensitive volumetric mechanism associated with both the gas temperature with T^4 dependence and combustion products as CO_2, H_2O, and soot. As a consequence, a larger buoyancy-induced fire size (Figure 5) enhances the radiation heat flux with an increase by a factor of two times compared to that from a flat microgravity flame, and 16 times that from a flame behind a backward-facing step.

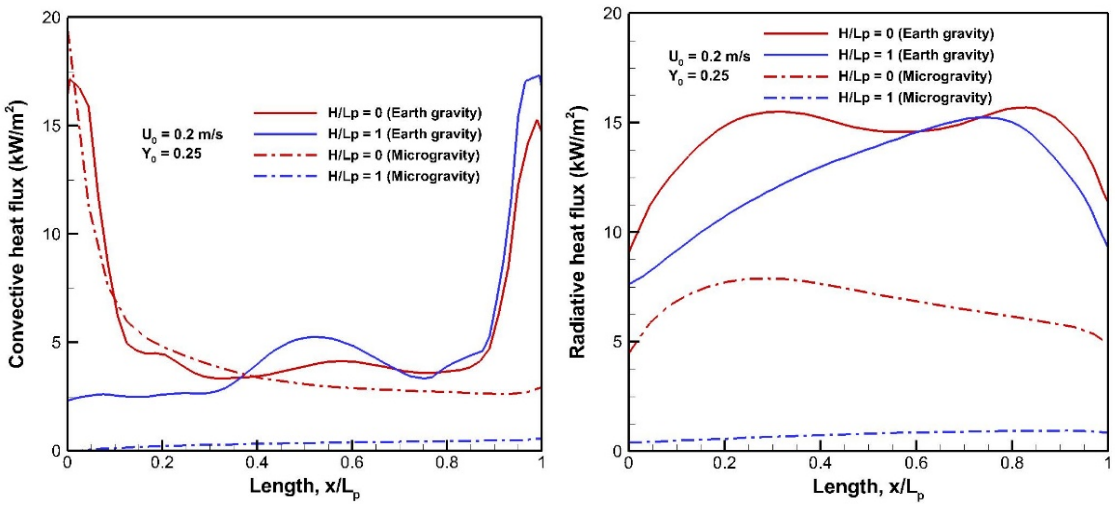

7a). Convection flux. 7b). Radiation flux.

Figure 7. Impact of gravity on the heat feedback from a flame to a fuel surface.

The ratio of the radiative heat flux to the total heat flux over the heptane surface is given in Figure 8 to identify the thermal regime for the fire growth. For the buoyancy-induced fire, the convection heat flux is dominant near the leading edge with a radiative fraction of about 40%, while a radiation fraction of 80% is maintained at the center of pyrolysis area as a result of a large buoyancy-induced thermal plume. Near the corner of a backward-facing step, the radiative fraction of the buoyancy-induced fire reaches about 80% due to a reduction in the temperature gradient. In the absence of natural convection, a radiative fraction is roughly 20% near the leading edge of a flat surface and, thus, flame growth is ensured thanks to substantial convective feedback. Downstream the leading edge, with an increase in thickness of the hotter boundary layer over a flat surface at microgravity, the radiation fraction reaches about 70%. For a microgravity flame behind a backward-facing step, the radiation heat feedback from

the flame to the condensed surface is the primary cause of fire growth with a radiative fraction higher than 70% due to the flame detachment from the pyrolysis surface.

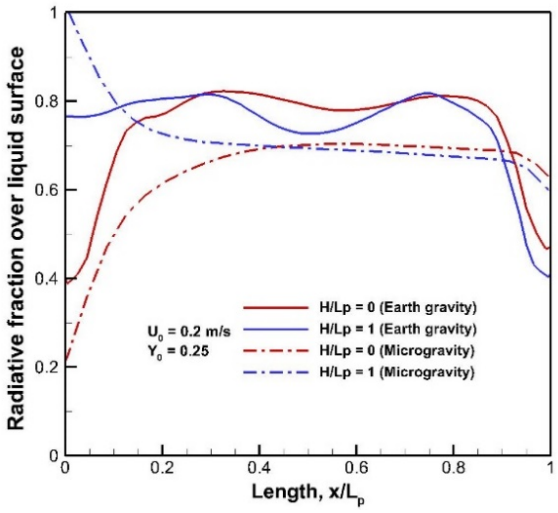

Figure 8. Impact of gravity on radiative fraction over the heptane surface.

The predicted temperature over the liquid surface at a steady state along the x axis on the central plane is provided in Figure 9. Although the convection heat flux is dominant with a high peak near the leading edge (Figure 7a), more cold air is entrained with a drop in liquid temperature. Liquid fuel in the middle section of the pyrolysis zone becomes easy to preheat with a higher temperature thanks to substantial luminous radiation. The liquid temperature shows a slowly growing trend for the flame behind a backward-facing step and reaches a peak near the tailing edge. The liquid temperature of buoyancy-induced fire is higher than that of a microgravity flame because of the enhanced heat flux (Figure 7) on Earth.

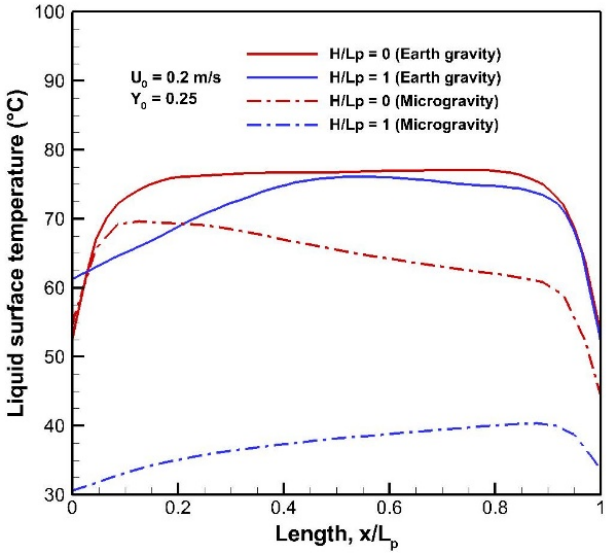

Figure 9. Impact of gravity on liquid surface temperature.

At a steady state, the evaporation rate asymptotically reaches a limit to supply a permanently burning flame once the liquid temperature is established over a liquid surface, as shown in Figure 10. In normal gravity, a peak in the evaporation rate takes place at the leading edge due to strong interaction between crossflow and buoyant driven flow, followed by its sharp decrease beyond that region. The possibility of reaching a low evaporation rate of about 1 g/m^{2}s is expected due to insufficient heat feedback from a microgravity flame behind a backward-facing step to increase liquid temperature (Figure 9). For a flat microgravity flame, the evaporation rate reaches a peak at the leading edge due to an enhancement of convection heat flux (Figure 7a), and decreases progressively to a small value. The buoyancy-induced fire (Figure 5) seems more pronounced compared to a microgravity flame (Figure 6), resulting in an increase of the evaporation rate by a factor of 2.3 times in the peak, mainly due to a contribution of radiative feedback (Figure 7b). A strong burning rate over a flat surface at microgravity contributes to an increase in flame length by a factor of 10 times in comparison with the flame length in the presence of a backward-facing step (Figure 6).

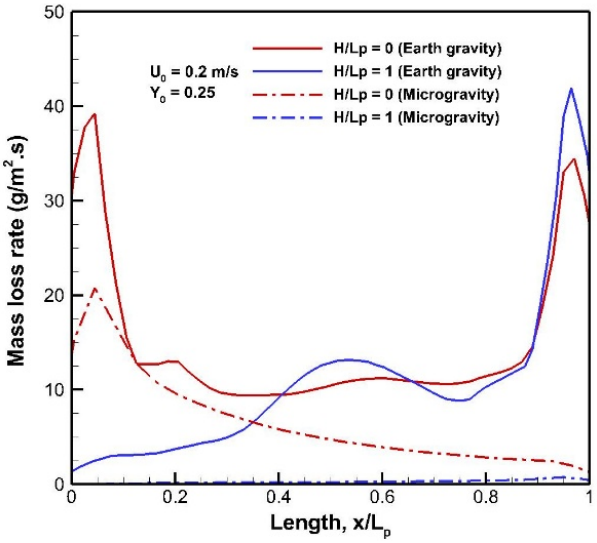

Figure 10. Impact of gravity level on the evaporation rate of heptane.

To further show the dependence of the flame behavior on the gravity, flame temperature, radiative loss fraction, HRR, and combustion efficiency are summarized in Table 1. For the buoyancy-controlled fire, the temperature peak seems insensitive to the presence of a backward-facing step in front of the flame with a peak above 1200°C. Behind a backward-facing step, a weak combustion intensity in microgravity with a regression rate of 1 g/m^{2}s significantly reduces the temperature peak to a critical value of 740°C below which no sustained flame exist [15]. Radiation heat transfer becomes predominant in the absence of natural convection with a higher radiative loss fraction above 0.5 compared to 0.35 for buoyancy-induced fire. The HRR derived from the evaporation rate (Figure 10) is normalized over the burning surface area, giving Heat Release Rate Per Unit Area (HRRPUA). For buoyancy-controlled fire, HRRPUA augments 1.5 times in comparison with that for a flame behind a backward-facing step. A rapid regression rate of a flat microgravity flame (Figure 10) contributes to a higher HRRPUA by a factor of 10 times in comparison with that for a flame behind a backward-facing step (Figure 6). The combustion efficiency can be evaluated from the ratio between the effective HRR,

which is determined from the chemistry model (Eqs.1–3), and the theoretical one, which is derived from the evaporation rate (Figure 10). Although a backward-facing step prevents transport of the fresh air into the reaction zone, a low pyrolysis rate (Figure 10) contributes to a high combustion efficiency of about 0.9.

Table 1. Dependence of the flame behavior on the gravity level.

	Microgravity (H/L_p=0)	Earth gravity (H/L_p=0)	Microgravity (H/L_p=1)	Earth gravity (H/L_p=1)
Flame temperature (°C)	1282	1216	740	1231
Radiative loss fraction	0.62	0.36	0.57	0.37
HRRPUA (kW/m^2)	215	676	21	470
Combustion efficiency	0.66	0.67	0.9	0.92

From the evaluation of smoke hazards, including CO and CO_2, to occupants [14], roughly 80% of fire fatalities is attributed to smoke/gas incapacitation. Distributions of CO on the symmetrical plane are depicted in Figure 11 and Figure 12. For a buoyancy-induced fire, most CO production takes place in an oxygen-starved, high temperature region around the pyrolysis zone. The buoyancy-entrained cold air conducts a sharp decrease of the CO emission in a thermal plume region. A flat microgravity flame carries abundant CO along the forward boundary layer with a slow decay of the CO emission due to a strong diffusion. It seems that the peak in CO molar fraction is weakly dependent on the presence of a backward-facing step in front of a fire with a maximum in a range from 1.5% to 1.7%, which is indicative of an equivalent fuel-air ratio in the reaction region.

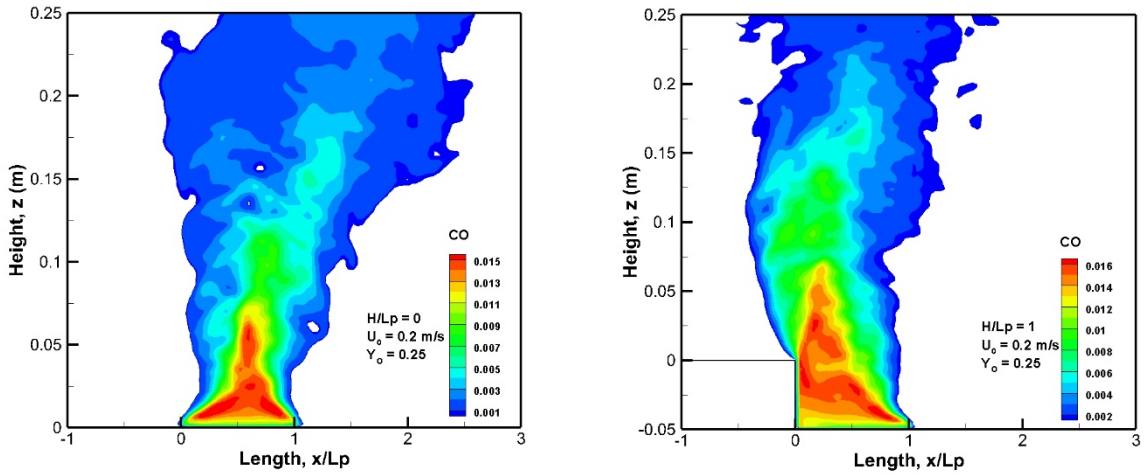

11a). Over a flat surface. 11b). Behind a backward-facing step.

Figure 11. Distributions of a CO molar fraction in normal gravity on the symmetrical plane (x, z).

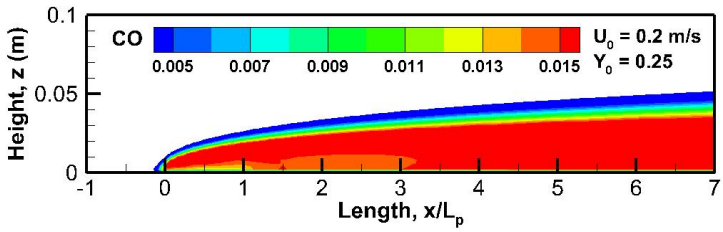

12a). Over a flat surface.

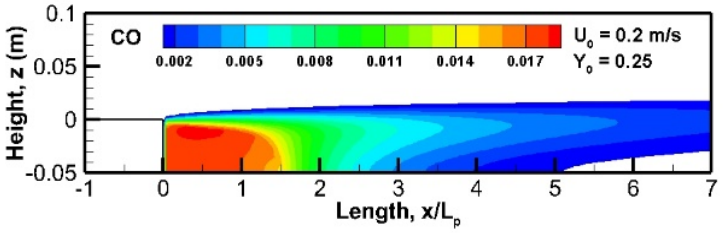

12b). Behind a backward-facing step.

Figure 12. Distributions of a CO molar fraction at microgravity on the symmetrical plane (x, z).

The volume of air breathed per minute during a fire depends on the concentration of inhaled CO_2 [14]. Figures 13 and 14 show the distributions of carbon dioxide concentrations on the symmetrical plane. For a buoyancy-induced fire, the CO_2 molar fraction is in abundance with a maximum of about 9% in a high chemical reactivity region following the trend of CO generation (Figures 11 and 12). A flat microgravity flame facilitates a large presence of CO_2 downstream along the boundary layer (Figure 6). For a microgravity flame behind a backward-facing step, the reduced convective transport of the fresh air into the reaction zone leads to an increase of CO_2 to 12% compared to 9% on Earth.

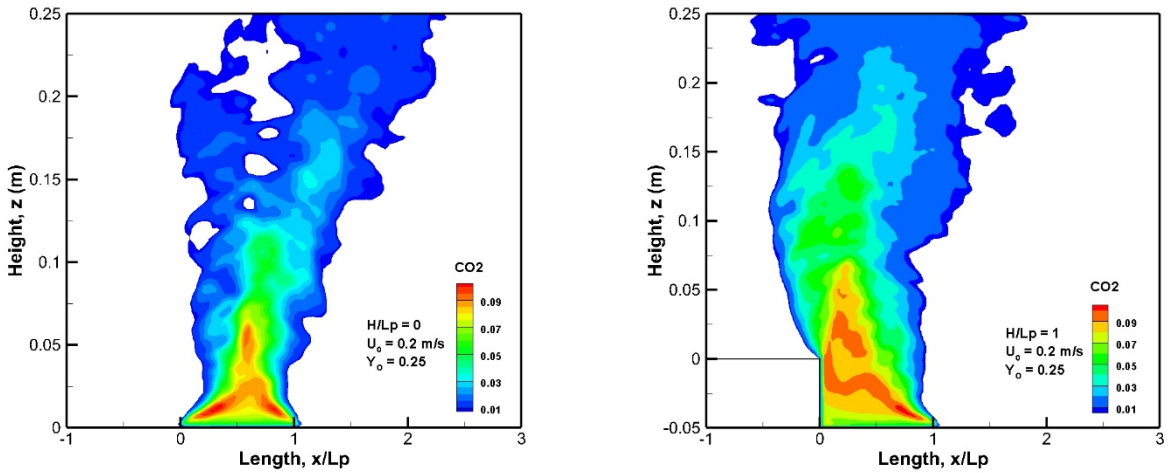

13a). Over a flat surface. 13b). Behind a backward-facing step.

Figure 13. Fields of CO_2 volume fraction in normal gravity on the symmetrical plane (x, z).

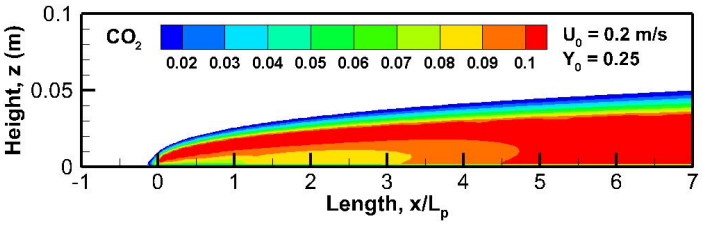

14a). Over a flat surface.

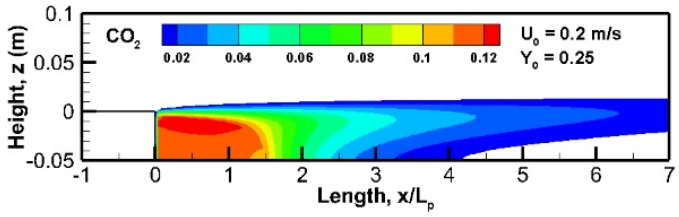

14b). Behind a backward-facing step.

Figure 14. Fields of CO_2 volume fraction in microgravity on the symmetrical plane.

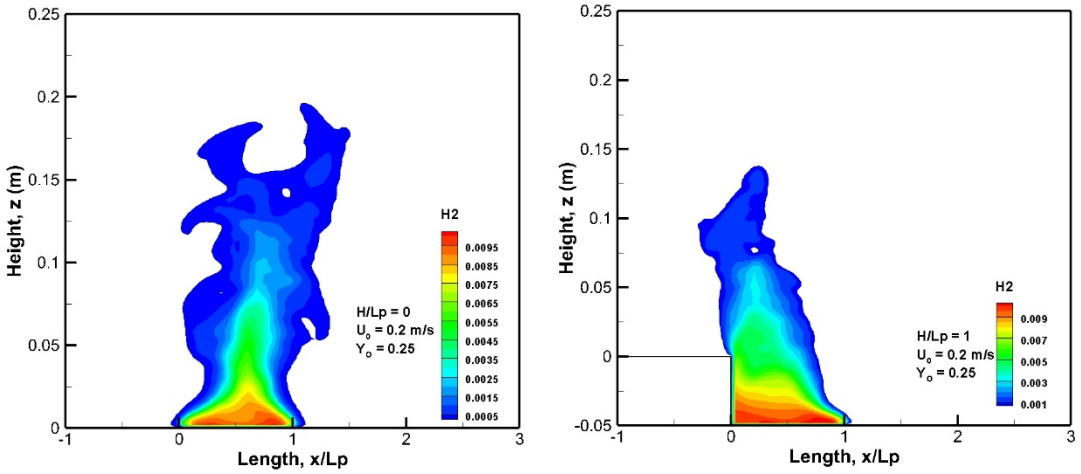

15a). Over a flat surface. 15b). Behind a backward-facing step.

Figure 15. Fields of hydrogen volume fraction in normal gravity on the symmetrical plane.

Distributions of hydrogen on the symmetrical plane (x, z) are depicted in Figures 15 and 16. For the buoyancy-induced fire, a high pyrolysis rate (Figure 10) correlates to a large extent of hydrogen concentrations above 0.5% within the high temperature region. The small evaporation rate for the microgravity flame behind a backward-facing step significantly reduces the H_2 formation due to a low flame temperature (Figure 6b). It is found that H_2 is generated only in a high chemical reactivity region where the temperature is sufficiently high. The peak of H_2 production for buoyancy-induced flame augments about two times in comparison with that for a flat microgravity flame. For the microgravity

flame behind a backward-facing step, the H_2 formation in the forward direction undergoes a low peak of 50 ppm due to a low chemical reactivity. Globally, hydrogen occurs only in the fuel-rich and oxygen-starved area at locations where the temperature is high enough to trigger its activation. In case of a fire, hydrogen will escape quickly into the atmosphere as a very diffuse gas and may burn spontaneously if it contains dust. Moreover, it is highly flammable with an ignition energy that is smaller than that of unburnt hydrocarbons [14].

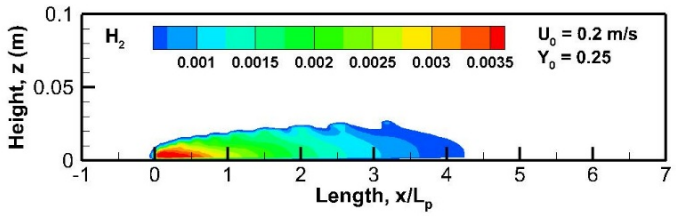

16a). Over a flat surface.

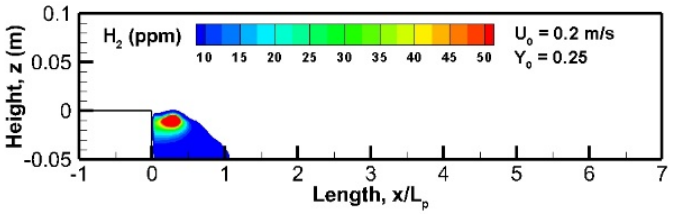

16b). Behind a backward-facing step.

Figure 16. Fields of hydrogen volume fraction in microgravity on the symmetrical plane.

A lack of oxygen near the pyrolysis zone leads to the formation of unburnt hydrocarbon as heptane, as depicted in Figure 17 and Figure 18 on the symmetrical plane (x, z). A plat microgravity flame with a strong evaporation rate leads to a peak of 20% in molar fraction of unburnt fuel near the pyrolysis surface. A reduced evaporation rate for the microgravity flame behind a backward-facing step enables us to maintain a low peak of about 10% in unburnt fuel at the tailing edge (x/L_p=1). Although a buoyancy-induced air entrainment enhances oxidation of the unburnt fuel into CO and CO_2, a strong pyrolysis rate (Figure 10) of liquid fuel correlates to a rise of molar fraction of the unburnt hydrocarbons to 38%. A decrease in the air supply toward the buoyancy-induced flame behind a backward-facing step reduces the slight generation of the unburnt hydrocarbons due to a low pyrolysis rate (Figure 10). Usually, an increase in CO production (Figures 11 and 12) follows the trend of unburnt hydrocarbons, which can be easily suppressed downstream once away from the fire source.

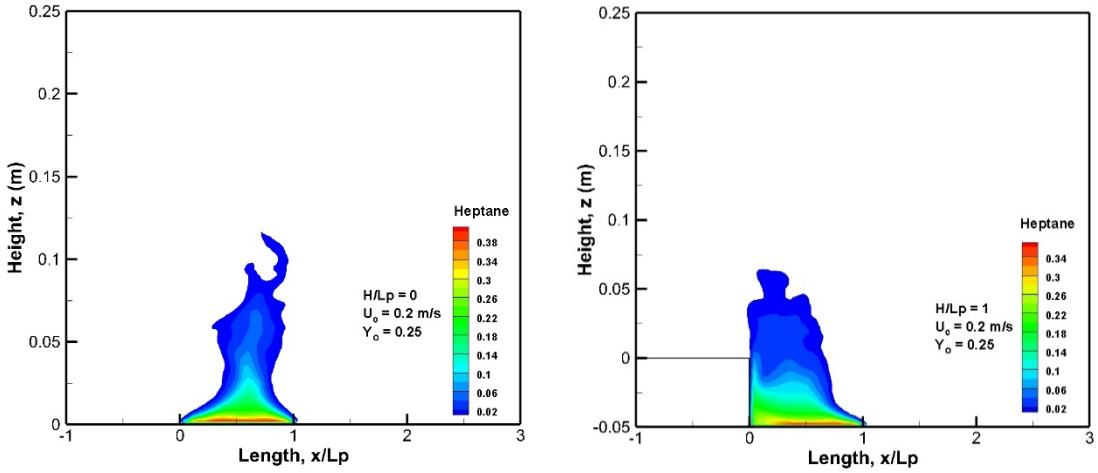

17a). Over a flat surface. 17b). Behind a backward-facing step.

Figure 17. Fields of unburnt fuel volume fraction in normal gravity on the symmetrical plane.

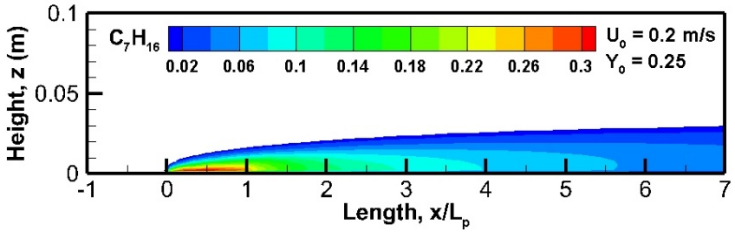

18a). Over a flat surface.

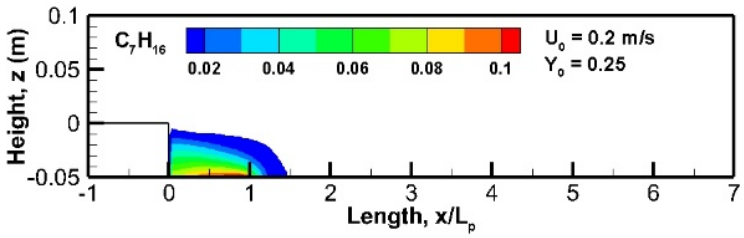

18b). Behind a backward-facing step.

Figure 18. Fields of unburnt fuel volume fraction in microgravity on the symmetrical plane.

The heptane fire is sootier, and its growth is significantly affected by the amount of soot via a great strength of flame radiation. Iso-contours of soot volume fraction on the symmetrical section are presented in Figure 19 and Figure 20. For a buoyancy-induced fire, few sooting regions are present near the burning surface, and most soot emission takes place in a high chemical reactivity region where heat is released. For a free-burning fire on Earth, the buoyancy-induced flow enhances the oxygen concentration at the leading edge with a low soot emission there, similar to that in [22]. Since the peak

in soot volume fraction is affected by the ratio between air entrainment and unburnt hydrocarbons, its peak seems insensitive to the presence of a backward-facing step on Earth. Moreover, natural convection is favorable for soot dilution in the thermal plume, and a flat microgravity flame tends to emit the abundant soot all along the boundary layer with an increase in the peak by a factor of 4 times. In the absence of natural convection, the excessive fuel with an additional evaporation rate of about 5 times over a flat plate (Figure 10) serves to conduct a heavy soot stratification thickness compared to the flame behind a backward-facing step.

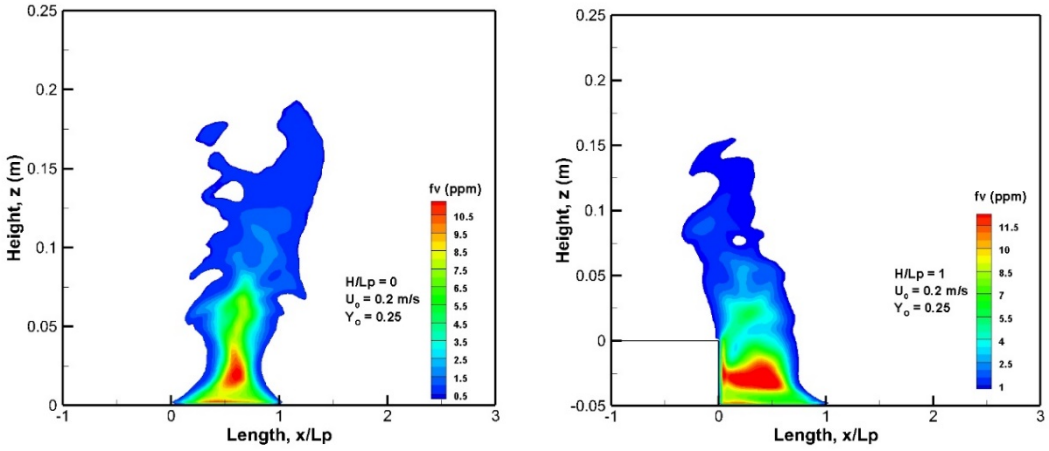

19a). Over a flat surface. 19b). Behind a backward-facing step.

Figure 19. Distributions of soot volume fraction in normal gravity on the symmetrical plane.

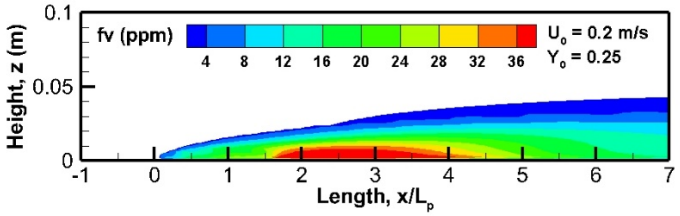

20a). Over a flat surface.

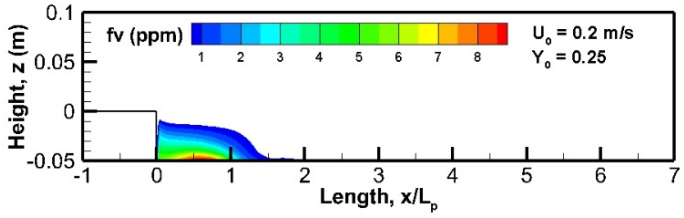

20b). Behind a backward-facing step.

Figure 20. Distributions of soot volume fraction at microgravity on the symmetrical plane.

Soot deposition from the gas-phase onto the wall surface reduces the visibility and increases the activation time for smoke detectors. As shown in Figure 21, the peak in soot deposition for buoyancy-induced fire occurs at the center of the evaporation zone (x/L_p=0.5), and a negligible soot deposition takes place near the leading edge. Notably, a backward-facing step in front of a buoyancy-induced fire reduces air entrainment, and, consequently, the peak in soot deposition takes place in the corner region where the thermal stratification (Figure 5b) and soot emission (Figure 19b) are significant. A flat microgravity flame conducts a significant soot deposition with a peak of 1.75 g/m^2 just downstream the trailing edge (x/L_p>1), and a complete absence of soot deposition occurs beyond x/L_p=7. In microgravity, the peak in soot deposition is about 6 times as high for a flame over a flat plate compared to a flame behind a backward-facing step. Compared to buoyancy-induced fire, the maximum soot deposition from a flat microgravity flame augments about 3 times due to a significant temperature gradient inside the boundary layer, which pushes soot particles approaching the wall surface via thermophoretical effects [28].

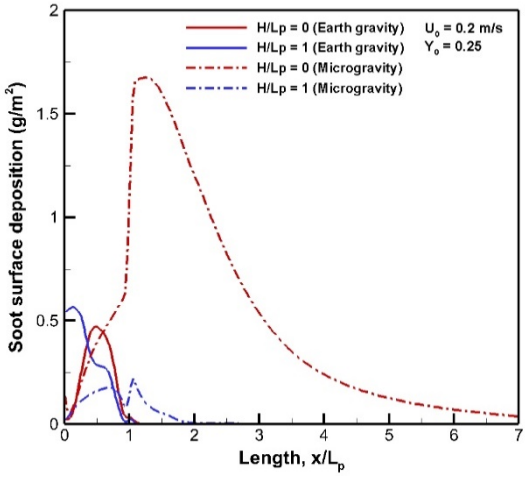

Figure 21. Impact of gravity on soot deposition (g/m^2) over a wall surface in the windward direction.

5. Concluding remarks

Significant results about the impact of gravity on flame shape, species compositions, and heat flux are provided, though they are limited in steady-state scope. For the fire growth over liquid fuel, the convective heat feedback is predominant at the leading edge, and the radiative heat transfer becomes a predominant mode far from that region. At least for the present configuration, the peak in evaporation rate is higher by a factor of two times in normal gravity than in microgravity due to the contribution of a large buoyancy-induced thermal plume at the base of the pyrolysis zone. However, the flame length is longer by a factor of about 2.5 times in a spacecraft than the flame height on Earth. Furthermore, a flat microgravity flame has much greater tendencies to emit the strongest soot with an increase in peak by a factor of about 4 times compared to the buoyancy-induced fire. As a result, the soot-related radiation contributes to a large and consistent radiative loss fraction in a range of 0.5 to 0.6 compared to about 0.35 for buoyancy-induced fire. A minimum buoyancy-induced flow dominates the behavior of the flame subjected to a low perpendicular flow velocity smaller than that on Earth. Therefore, a backward-facing step in front of a flame has a weak influence on both the chemical

characteristics and the heat flux on Earth, and the flame behavior exhibits a similarity. While a backward-facing step has a profound effect on the microgravity flame, which becomes weak and shorter in length. Oxygen starvation behind a backward-facing step induces a significant flame shift at microgravity outward from the evaporation surface with a neglected convective heat transfer.

It is worth noting that the uncertainty in the calculated soot stratification thickness for a heptane flame is estimated within two times in an inadequate oxygen region where soot burnout via O* and OH* radicals become predominant. Based on a multi-step, quasi-global mechanism, it is difficult to determine how accurate the theoretically predicted chemical species concentration is because of potential changes with different kinetic reaction mechanisms. The verification of theoretical models on chemical species with velocities lower than that induced by buoyancy over a heptane surface is limited because the valuable experimental data in microgravity are rare because of the difficulty to conduct long-term experiments. In a future study, we aim to obtain more potential experimental data on the liquid vaporization rate, heat flux over a liquid surface, and chemical species, which could support the simulation results by using a detailed chemical mechanism for combustion and soot modeling.

Author contributions

Investigation: Wang Hui Ying, Anh Quan Nguyen; Writing, supervision: Wang Hui Ying; Software for all the figures: Anh Quan Nguyen; Analysis of the results: Wang Hui Ying, Anh Quan Nguyen.

Use of AI tools declaration

The authors declare they have not used Artificial Intelligence (AI) tools in the creation of this article.

Acknowledgements

The present research was supported by the French government program: France 2030 (LABEX INTERACTIFS, reference ANR-11-LABX-0017-01).

Conflict of interest

The authors declare no conflict of interest.

Data Availability

The datasets generated during the current study are available from the corresponding author on reasonable request.

References

1. Jomaas G, Torero JL, Eigenbrod C, et al. (2015) Fire safety in space–beyond flammability testing of small samples. *Acta Astronaut* 109: 208–216. https://doi.org/10.1016/j.actaastro.2014.11.025
2. Friedman R (1996) Fire Safety in Spacecraft. *Fire Mater* 20: 235–243. https://doi.org/10.1002/(SICI)1099-1018(199609)20:5<235::AID-FAM580>3.0.CO;2-Y

3. Link S, Huang X, Fernandez-Pello C, et al. (2018) The effect of gravity on flame spread over PMMA cylinders. *Sci Rep* 8: 120. https://doi.org/10.1038/s41598-017-18398-4
4. Roslon M, Olenick S, Zhou YY, et al. (2001) Microgravity ignition delay of solid fuels in low-velocity flows. *AIAA J* 39: 2336–2342. https://doi.org/10.2514/2.1239
5. Fernandez-Pello AC, Ray SR, Glassman I (1978) Downward flame spread in an opposed forced flow. *Combust Sci Technol* 19: 19–30. https://doi.org/10.1080/00102207808946860
6. Johnston MC, James S, Muff DE, et al. (2015) Self induced buoyant blow off in upward flame spread on thin solid fuels. *Fire Safety J* 71: 279–286. https://doi.org/10.1016/j.firesaf.2014.11.007
7. Delichatsios MA, Altenkirch RA, Bundy MF, et al. (2000) Creeping flame spread along fuel cylinders in forced and natural flows and microgravity. *P Combust Inst* 28: 2835–2842. https://doi.org/10.1016/S0082-0784(00)80706-7
8. Smirnov NN, Tyurenkova VV, Smirnova MN (2015) Laminar diffusion flame propagation over thermally destructing material. *Acta Astronaut* 109: 217–224. https://doi.org/10.1016/j.actaastro.2014.09.016
9. Carmignani L, Dong K, Bhattacharjee S (2020) Radiation from flames in a microgravity environment: experimental and numerical investigations. *Fire Technol* 56: 33–47. https://doi.org/10.1007/s10694-019-00884-y
10. Ferkul P, Kleinhenz J, Shih H Y, et al. (2004) Solid fuel combustion experiments in microgravity using a continuous fuel dispenser and related numerical simulations. *Microgravity Sci Tec* 15: 3–12. https://doi.org/10.1007/BF02870953
11. Nagachi M, Citerne JM, Dutilleul H, et al. (2021) Effect of ambient pressure on the extinction limit for opposed flame spread over an electrical wire in microgravity. *P Combust Inst* 38: 4767–4774. https://doi.org/10.1016/j.proci.2020.05.005
12. Donzeau M, Esclapez L, Day M, et al. (2023) Recent Progress on Numerical Modeling for Microgravity Electric Field Flames, 1*3th U.S. National Combustion Meeting, College Station*, Texas, 19–22.
13. Kumar V, Prema Prescilla T, Kumar A, et al. (2024) An Experimental Study of Opposed Flame Spread along Various Thin Fuel Configurations in Microgravity. *Microgravity Sci Tec* 36: 64. https://doi.org/10.1007/s12217-024-10147-3
14. Hurley MJ (2016) SPFE Handbook of Fire Protection Engineering, *Fifth Edition, National Fire Protection Association*, Springer New York, Chapter 18: 554–580 and Chapter 21: 633–661, Chapter 63: 2308–2414.
15. Ross HD, Miller FJ (2000) Understanding flame spread across alcohol pools, *Proceedings of the sixth international symposium*, Poitiers, France: International Association for Fire Safety Science, 77–94.
16. Ross HD, Miller FJ (1998) Flame spread across liquid pools with very low-speed opposed or concurrent airflow, *Symposium (International) on Combustion*, Elsevier, 27: 2723–2729. https://doi.org/10.1016/S0082-0784(98)80128-8
17. Brohez S, Saladino D, Perelli M (2022) Experimental and Numerical Study of Heptane Pool Fire. *Chem Eng T* 91: 223–228. https://doi.org/10.3303/CET2291038
18. Cavazzuti M, Tartarini P (2024) Pool Fires Within a Large Under-Ventilated Environment: Experimental Analysis and Numerical Simulation Using OpenFOAM. *Fire Technol* 60: 1891–1915. https://doi.org/10.1007/s10694-024-01554-4

19. Jiusheng Y, Wei Y, Quanyi L, et al. (2013) Experimental study of n-heptane pool fire behaviors under dynamic pressures in an altitude chamber. *Procedia Eng* 52: 548–556. https://doi.org/10.1016/j.proeng.2013.02.184
20. Beji T, Zhang JP, Delichatsios M (2008) Determination of soot formation rate from laminar smoke point measurements. *Combust Sci Technol* 180: 927–940. https://doi.org/10.1080/00102200801894398
21. McGrattan K, Hostikka S, McDermott R, et al. (2013) Fire dynamics simulator user's guide (sixth ed.). *NIST special publication* 1019: 1–339.
22. Acherar L, Wang HY, Coudour B, et al. (2023) Assessment of Semi-Empirical Soot Modelling in Turbulent Buoyant Pool Fires from Various Fuels. *Thermo* 3: 424–442. https://doi.org/10.3390/thermo3030026
23. Wang HY (2022) Impact of fuel type on toxic emissions from a non-premixed boundary layer laminar flame in microgravity–a numerical study. *Microgravity Sci Tec* 34: 94. https://doi.org/10.1007/s12217-022-10011-2
24. Cox G (1995) Combustion fundamentals of fire, Academic Press INC.
25. Murty KA (1984) Introduction to Combustion Phenomena, New York: Gordon.
26. Guibaud A, Consalvi JL, Orlac'h JM, et al. (2020) Soot production and radiative heat transfer in opposed flame spread over a polyethylene insulated wire in microgravity. *Fire Technol* 56: 287–314. https://doi.org/10.1007/s10694-019-00850-8
27. Lee KB, Thring MW, Beer JM (1962) On the rate of combustion of soot in a laminar soot flame. *Combust Flame* 6: 137–145. https://doi.org/10.1016/0010-2180(62)90082-2
28. Fuentes A, Legros G, Claverie A, et al. (2007) Influence of the oxidizer velocities on the sooting behaviour of non-buoyant laminar diffusion flame, *31th Symposium (International) on Combustion*, Pittsburgh: The Combustion Institute, 2685–2692.
29. Torero JL, Bonneau L, Most JM, et al. (1994) The effect of gravity on a laminar diffusion flame established over a horizontal flat plate, *Symposium (International) on Combustion*, Elsevier, 25: 1701–1709. https://doi.org/10.1016/S0082-0784(06)80818-0
30. Glassman I, Yetter RA, Glumac NG (2014) *Combustion*, Academic press.
31. Olson SL (1991) Mechanisms of microgravity flame spread over a thin solid fuel: oxygen and opposed flow effects. *Combust Sci Technol* 76: 233–249. https://doi.org/10.1080/00102209108951711

AIMS Press